LA-UR- 08-6527

Approved for public release; distribution is unlimited.

Title:	In-situ Time-Resolved Neutron Diffraction Measurements of Microstructure Variations during Friction Stir Welding in a 6061-T6 Aluminum Alloy
Author(s):	W. Woo, Z. Feng, C. R. Hubbard, X-L. Wang and S. A. David, Oak Ridge National Laboratory, Oak Ridge, TN, USA B. Clausen, Los Alamos National Laboratory, Los Alamos, NM, USA T. Ungár, Eötvös University, Budapest, Hungary
Intended for:	Proceedings paper from the 2008 Trends in Welding Research, 6/1-6/2008, Pine Mountain, Georgia, USA

Form 836 (7/06)

In-situ Time-Resolved Neutron Diffraction Measurements of Microstructure Variations during Friction Stir Welding in a 6061-T6 Aluminum Alloy

W. Woo, Z. Feng, C. R. Hubbard, and S. A. David
Materials Science and Technology Division, Oak Ridge National Laboratory, Oak Ridge, TN, USA

X-L. Wang,
Spallation Neutron Source, Oak Ridge National Laboratory, Oak Ridge, TN, USA

B. Clausen
Los Alamos Neutron Science Center, Los Alamos National Laboratory, Los Alamos, NM, USA

T. Ungár
Department of Materials Physics, Eötvös University, Budapest, Hungary

Abstract

The microstructure change is one of the most important research areas in the friction stir welding (FSW). However, in-situ observation of microstructure changes during FSW has been extremely challenging because many measurement techniques are inapplicable. Recently developed in-situ time-resolved neutron diffraction method, which drastically improves the temporal resolution of neutron diffraction, enables to observe the transient microstructure changes during FSW. We installed a portable FSW system in the Spectrometer for MAterials Research at Temperature and Stress (SMARTS) at Los Alamos Neutron Science Center and the FSW was made on 6.35mm-thickness 6061-T6 Al alloy plate. At the same time, the neutron beam was centered on the mid-plane of the Al plate at 8 mm from the tool center (underneath the tool shoulder) and the diffraction peak was continuously measured during welding. The peak broadening analysis has been performed using the Williamson-Hall Method. The result shows that the dislocation density of about 3.2×10^{15} m^{-2} in that position *duing* FSW, which is the significant increse compared to the *before* (4.5×10^{14} m^{-2}) and *after* (4.0×10^{14} m^{-2}) the FSW. The quantitatively analysis of the grain structure can provide an insight to understand the transient variation of the microstructure during FSW.

Introduction

Friction-stir welding (FSW) is a solid-state joining process utilizing a rotating tool consisting of a threaded pin and tool shoulder that applies severe plastic deformation and frictional heating into the joining materials [1]. The benefits and uniqueness of the FSW have been well established for many light-weight metals and alloys that have difficulties in joining by the conventional fusion welding methods [2]. The frictional heat and severe plastic deformation involved in the FSW, however, causes significant changes in the microstructure of heat-treatable Al alloys. Extensive research work has been performed on FSW heat-treatable Al alloys to understand the microstructure (precipitates, grain size, and dislocations) [3-7] and its influence on the mechanical properties such as yield strength, ductility, and strain hardening behavior [8-10].

In many engineering processes, severe plastic deformation results in a large amount of dislocations in microstructure [11-13]. It has also been reported that the dislocation-embedded 'grain structure' is subjected to lattice distortions and strains within grains [14,15]. For FSW, the grain structure is also influenced by the severe plastic deformation and annealing process such as recovery and/or recrystallization at elevated temperatures during welding [3-7].

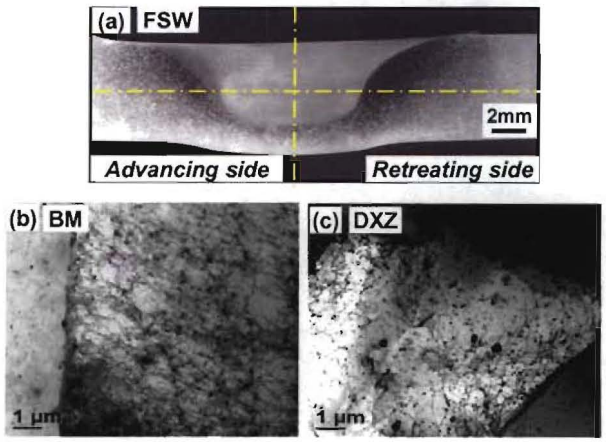

Figure 1: Microscopy of the friction stir welded 6061-T6 Al alloy. (a) Macrostructure of the cross-section in FSW. TEM bright-field images of: (b) the base material (BM) and (c) the dynamic recrystallized zone (DXZ). The black line segments and dots indicate dislocations and precipitates in grain structure, respectively.

As an illustration, the optical microscopy of FSW and the two bright-field Transmission Electron Microscope (TEM) images are given in Fig. 1. The TEM images show the typical dislocation-embedded microstructure, often called grain structure, in a commercial rolled aluminum alloy plate (base material), Fig. 1b. It is evident that the as-received Al plate sample contains a large number of dislocations shown as black line segments. Meanwhile, the FSWed Al metal shows relatively less dislocations in grains due to the dynamic recrystallization during FSW. These conventional TEM observations rely on the "post-mortem" analysis method, which examines the material after processing. Herein, we motivate to examine the materials behavior "during" processing. Therefore, in-situ real-time observations of the microstructural features connect each step of the transient microstructure to the final state. In-situ observations can provide the knowledge-based microstructure through the control of the processing variables for the superior mechanical properties.

Consequently, the better understanding of the grain structure in FSW, i.e., detailed information on the dislocation density and subgrain size, is necessary since the grain structure can significantly affect the plastic deformation behavior such as strain hardening rate and hardening capacity in the FSW [16,17]. However, although the grain morphologies and dislocation structures have been observed on various FSW alloys using TEM and other methods, very limited quantitative analysis of the grain structure in terms of the dislocation density and subgrain size is available up to date.

In this paper, we present the dislocation density and subgrain size in a FSW 6061-T6 Al alloy measured by in-situ time-resolved neutron diffraction. The measured diffraction peaks will be analyzed using the peak broadening analysis of diffraction profiles. The variations of the subgrain size and dislocation density will be observed and compared among the three different cases: *before*, *during*, and *after* the FSW.

Experimental details

As-received commercial 6061-T6 Al alloy rolled plate was solution-heat treated and aged for 6 hours at 185°C. The nominal chemical composition in weight percent is 1.0 Mg, 0.6 Si, 0.3 Cu, and balance Al. Grains of about 200-μm size were elongated along the rolling direction with a typical recrystallized rolling texture. The cross-section of the FSW plate was cold-mounted, polished, and etched with the Keller's reagent for the optical microscopy at room temperature. The grain structure was observed using conventional TEM. Disc type specimens prepared by electrical discharge machine (EDM) were mechanical grinded to 100 μm thickness of foil, and electropolished using a 30% nitric acid solution in methanol with 25 voltages for 20 seconds at -30 °C.

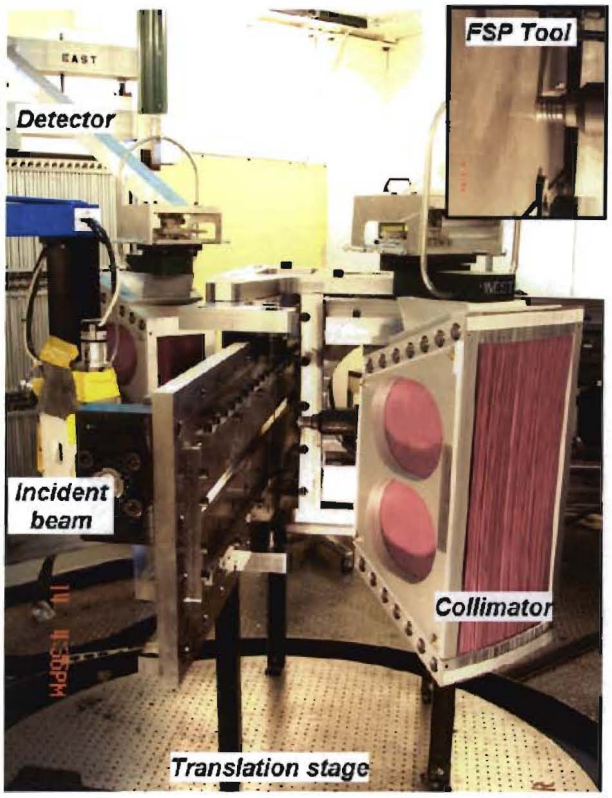

Figure 2: Experimental setup of the in-situ time-resolved neutron diffraction measurement during FSW. The FSW machine was mounted on the X-Y translation stage of SMARTS [18] neutron diffractometer and real time measurements were performed as the deformation region was being made along the horizontal arrangement of the machine. The inset presents the FSW stirring tool contacting on the Al 6061-T6 plate during FSW.

We specially designed a friction-stir welding machine in real engineering scale, Fig. 2. The softened materials by heat underneath the rotating tool shoulder flow around the tool pin column with pressure and consolidate behind the tool to form a solid-state continuous region. The hard tool made of an H-13 steel and the diameter of the threaded pin and the tool shoulder was 6.35 and 25.4 mm, respectively. The specimen of the Al plate has 965-mm long (x), 178-mm wide (y), and 6.35-mm thick (z) dimension. The machine with the specimen was mounted on the translation stage of SMARTS and remotely operated. The whole plate sample continuously traverses at a constant traveling speed of 0.42 mm/s simultaneously as the tool is rotating (156 revolutions/min) with a pressure into the sample surface to impose the severe thermo-mechanical deformation on materials. The transverse sides of the plate sample was clamped to constrain the displacement during processing and the clamping was removed after air cooled to 25 °C. In the end, a 760-mm long and 25-mm wide deformation region was made along the middle of the plate width.

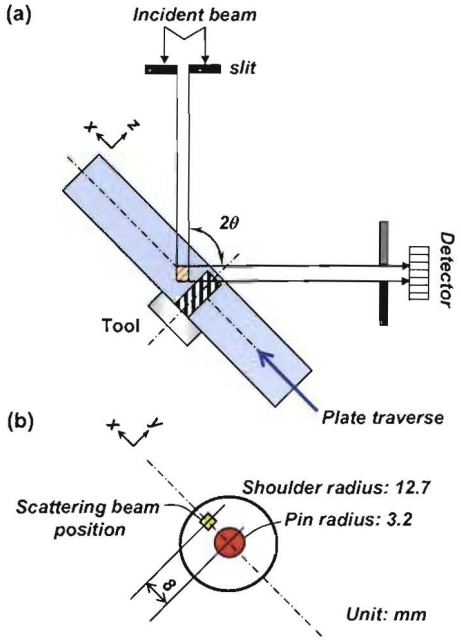

Figure 3: (a) Sketch of the in-situ time-resolved neutron-diffraction experiment (top view). As the rotating FSW tool imposes the severe thermo-mechanical deformation on sample, the neutron diffraction peaks were simutaneously measured at the detector. (b) Location of the neutron diffraction measurement during FSW. The neutron beam scattering volume was predetermined at 8 mm behind the tool center (underneath the tool shoulder).

The neutron diffractgion has a unique deep penetration capability into most metals. Note that over 12-mm penetration is necessary through the steel tool and Al plate for the beam path in the current study. However, the relatively weak neutron fluxes cause difficulties in the in-situ experiments. Thus, in-situ neutron diffraction study of dynamic materials behavior requires a completely different experimental approach from the conventional study of static problems such as residual stress measurements [19]. We measured the transient diffraction peaks based on the quasi-steady state (QSS) phenomenon [20]. The QSS is an energy equilibrium state, which is not changing of the materials behavior as a function of time. This QSS phenomenon can be found in many material processing technologies such as joining, casting, solidification, and growth of single crystal. The required temporal resolution (~ 20 min) of the typical neutron-diffraction measurements can be achieved when utilizing the QSS phenomenon [21]. In order to create the QSS, importantly, the whole Al sample plate was continuously traversed along the x-direction and simultaneously the neutron diffraction measurements were performed as the deformation zone was being made, Fig. 3(a). The incident neutron beam was focused on the predetermined measurement location (8 mm behind the tool center) and the detector collected the diffraction peaks from the defined scattering volume with their scattering vectors parallel to the normal direction of the plate using the scattering volume (2 x 2 x 3 mm^3) defined by the 2 (x) x 2 (y) mm^2 square slit of the incident beam and the 3-mm (z) wide radial collimator. The long plate sample dimension (965-mm long) allowed achieving over 20 minutes of the QSS during FSW and, thereby dissolved the limitation of the temporal resolution in neutron diffraction measurements. It should be noted that the neutron diffraction measurements were performed from the base material (*Before* FSW) for 2 hours (obtaining the sufficient peak intensities) and from the DXZ (*After* FSW) for about 6 hours when the sample completely cools down.

Results and discussion

Neutron diffraction peaks analysis

In order to study the transient materials behavior as the materials exits the deformation region, the diffraction peaks were measured underneath tool shoulder during FSW. The raw data of the diffraction peaks was fitted using Rietveld peak refinement in the General Structure Analysis System (GSAS) [22]. The Rietveld refinement analyzes the entire diffraction profile by comparing the measured profile and calculated one based on the crystallographic space group. It determines the interplanar spacing (d-spacing) of the material, Fig. 4. The d-spacing changes physically imply the expansion or contraction of the lattice plane. Compared to the initial d-spacings (*Before*), the results show the noticeable increases of the d-spacings during FSW (*During*) and those were gradually decreased when the sample was completely cooled down (*After*).

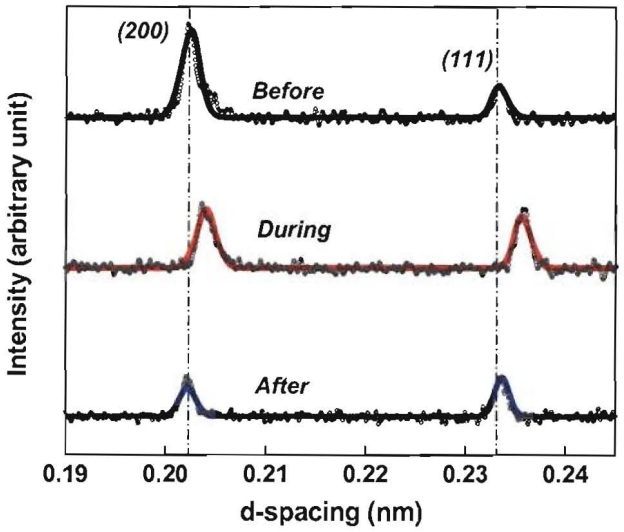

Figure 4: Neutron diffraction patterns in the (111) and (200) reflections. The gray dots indicate the directly measured neutron diffraction results and the overlapped profiles are Rietveld peak refinements. The neutron diffraction patters were measured from the base material (Before), during FSW (During), and when the FSW Al plate was completely cooled down (After).

Such trend correlates to the expected temperature variations: the highest thermal expansion near the heat source causing in the largest increase in d-spacing [23,24]. In addition, the peak intensity changes among (*hkl*) planes can be related to the dynamic texture evolution under FSW. Repeated measurements made during FSW at the same position confirmed the highly repeatable experimental conditions.

The diffraction peak profiles broaden when subgrains (coherent scattering domains called crystallites) are small or if the crystal lattice is distorted by lattice defects, especially by dislocations [15]. The FWHM (full width at half maximum) is defined as the diffraction peak width at half the peak height [15]. The higher FWHM indicates the broadened peak profile. The FWHM of the measured peaks as shown in Fig. 4 was analyzed using the single peak fitting method, which refines each (*hkl*) reflection of the measured diffraction peaks in GSAS. The FWHM results is summarized in Table 1(a). Compared to the initial state (*before*), the FWHM clearly increased during FSW (*during*). Such broadening of the FWHM is likely due to the microstructure changes: the highly introduced amounts of dislocations and the formation of small subgrains due to the severe thermo-mechanical deformation during FSW [5,6].

Table 1: Neutron diffraction analysis results: (a) full width at half maximum (FWHM) from (111) and (200) reflections, (b) subgrain size and (c) dislocation density. Neutron diffraction results were compared among the cases (Before, During, and After the FSW).

	(a) FWHM (nm)		(b) Subgrain size (nm)	(c) Dislocation density (m^{-2})
	(111)	(200)		
Before	0.00106	0.00094	120	4.5×10^{14}
During	0.00132	0.00171	160	3.2×10^{15}
After	0.00108	0.00095	130	4.0×10^{14}

Williamson-Hall peak broadening analysis

The diffraction peak profile analysis is a well-established technique for the determination of microstructure in crystalline materials [14,25]. The Williamson-Hall suggests that broadening of the diffraction peak profile (ΔK, nm^{-1}) can be written as a combination of the grain size ($0.9/D$) and strain (ΔK^D) effects [14]: $\Delta K = 0.9/D + \Delta K^D$ where $K = 1/d$, $\Delta K = -K(\Delta d/d)$, and D is the average subgrain size. The d (nm) is the d-spacing and Δd (nm) is the FWHM obtained from the single peak fitting of the diffraction data as shown in Table 1(a). Strain anisotropy in the conventional Williamson-Hall plot, Fig. 5(a), has been rationalized as replacing K by K^2C in the modified Williamson-Hall plot, Fig. 5(b), based on the following equation [25]:

$$(\Delta K)^2 \cong (0.9/D)^2 + (\pi A^2 b^2/2)\ \rho\ K^2C + O(K^2C)^2 \qquad (1)$$

where A is a constant depending on the effective outer cutoff radius of dislocations, b is the Burgers vector of dislocation (0.286 nm in Al), ρ is the dislocation density, and O indicates non-interpreted higher-order terms. Note that the C is the dislocation contrast factor, which can be determined by the elastic anisotropy and the dislocation type of materials [26]. Note that the average dislocation contrast factor (C_{hkl}) become a linear function of the (*hkl*) invariant of the reflections In the polycrystalline fcc Al metal: $C_{hkl} = 0.2[1-q(h^2k^2+h^2l^2+k^2l^2)/(h^2+k^2+l^2)^2]$, where the 0.2 is the average dislocation contrast factor for *h00* reflections. The contrast factor (0.2) was determined using the Fig. 1 of ref. 26 and the A parameter was calculated as 0.6 using the high-resolution x-ray diffraction measurement [27].

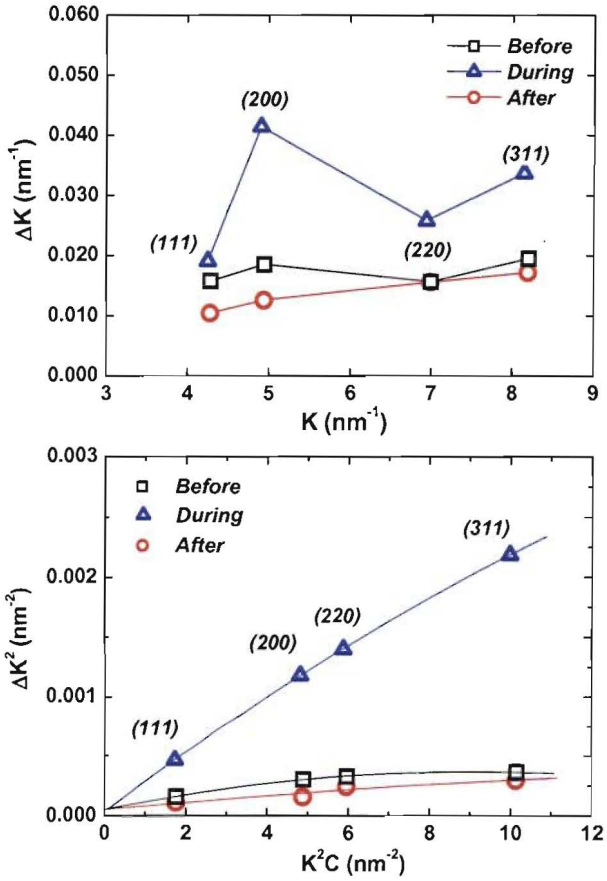

Figure 5: Peak broadening analysis using the Williamson-Hall plot. (a) The conventional and (b) the modified Williamson-Hall plot. The FWHM (full width at half maximum) was analyzed at Before, During, and After FSW. The K is defined as 1/d (d is the d-spacing in each hkl peak) and ΔK is driven as -K(Δd/d) (Δd is the FWHM obtained in neutron diffraction peak). The modified Williamson-Hall plot including the dislocation contrast factor (C). The interception of the fitted curve provides a subgrain size (when K = 0 in Eq. 1) and the slope of the fitting curve determines the dislocation density.

The modified Williamson-Hall plot clearly shows that the line broadening (ΔK) is more significant *during* FSW compared to the *before* and *after* FSW in each (*hkl*) peak. The modified Williamson-Hall plot provides two important microstructural features in the FSW [25,28]. First, the slope of the linear regression is proportional to the microstrain. The slope corresponding to the during FSW measuremt is considerably larger than that of the before and after FSW, indicating much larger microstrains caused by dislocations during FSW. Second, the intercept of the linear regression through the data points at $K = 0$ is a rough size estimation of the coherent scattering domains, indicating the similar average subgrain size among the three different cases.

Subgrain size and dislocation density

The analyzed subgrain size using the modified Williamson-Hall plot at the three different cases (*before*, *during*, and *after*) was summarized in Table 1(b). It has been reported that the crystallite or particle size obtained using diffraction methods can be equivalent (or similar) to the mean size of domains such as sub-grains or dislocation cells due to the coherently scattered x-rays or neutrons from such domains [15,28]. Consistently, it is clear that the subgrain size (nm scale) measured by the neutron diffraction, Table 1(b), is much smaller than the grain size (μm scale), which could be found in the literature [2]. It shows there is no significant increases in the sub grain size (160 nm) during FSW compared to the subgrain size before (120 nm) and after (130 nm) FSW Al 6061-T6 alloy.

Dislocation density can be closely related to the straining due to the severe plastic deformation and the recrystallization process during FSW [4-6]. Table 1(c) shows the variations of the dislocation density. Compared to the initial dislocation density (4.5×10^{14} m^{-2}), which could be found in the typical as-received rolled Al plate [29], the dislocation density significantly increased (3.2×10^{15} m^{-2}) during FSW, which was measured at 8 mm from the tool centerline and underneath the tool shoulder. It follows the decrease of the dislocation density to 4.0×10^{14} m^{-2} after FSW. The variation of the subgrain size and the dislocation density could be determined through the complicate FSW procedure such as the subdivision of grains, the dynamic recrystallization process, and the subsequent grain growth under the elevated temperature [5,6]. Such grain structure varations can be important to understand the deformation behavior, e.g., strain hardening, associated with the accumulation and interaction of the dislocations under FSW [30].

Summary

The variations of the subgrain size and dislocation density were determined in 6061-T6 Al alloy in the three different cases: *before*, *during*, and *after* the friction stir welding. The in-situ time-resolved neutron diffraction measurement method and the peak broadening analysis of the diffraction profiles using the modified Williamson-Hall plot quantifies the dislocation density of about 3.2×10^{15} m^{-2} and the average crystallite size of about 160 nm during FSW. The dislocation density during FSW is 7 times higher than the initial dislocation density measured from the base material (*before*) due to the severe plastic deformation of the FSW. Considered the clearly decreased dislocation density after FSW (*after*), it is believed that the dynamic recrystallization process causes significant decreases of the dislocation density in the recrystallized zone at the elevated temperature under FSW. This study shows the fast, transient dislocation density and subgrain size changes inside a bulk Al alloy during FSW providing a pathway by which the microstructure evolved.

Acknowledgements

This research is sponsored by the Laboratory Directed Research and Development program of Oak Ridge National Laboratory, managed by UT-Battelle, LLC for the U. S. Department of Energy under Contract No. DE-AC05-00OR22725. This work has a benefit from the use of the Lujan Neutron Scattering Center at Los Alamos National Laboratory funded by the Department of Energy's Office of Basic Energy under DOE contract DE-AC52-06NA25396. TEM work has a benefit by Research at the Oak Ridge National Laboratory SHaRE User Center supported by the Division of Materials Sciences and Engineering, Office of Basic Energy Sciences, U.S. Department of Energy, under Contract No. DE-AC05-00OR22725 with UT-Battelle, LLC. Authors thank H. Choo, E. A. Kenik, K. An, Y. Yamamoto, P. K. Liaw, J. Babb, S. Packer, and W. B. Bailey.

References

1. M.W. Mahoney, C.G. Rhodes, J.G. Flintoff, R.A. Spurling, and W.H. Bingle, *Mater. Trans. A* 29, 1955-64 (1998).
2. R.S. Mishra and Z.Y. MA, *Mater. Sci. Eng. R* 50, 1-78 (2005).
3. L.E. Murr, G. Liu, and J.C. Mcclure, *J. Mater. Sci.* 33, 1243-51(1998).
4. K.V. Jata and S.L. Semiatin, *Scripta Mater.* 43, 743-49 (2000).
5. J.Q. Su, T.W. Nelson, R. Mishra, and M. Mahoney, *Acta Mater.* 53, 713-29 (2003).
6. P.B. Prangnell and C.P. Heason, *Acta Mater.* 53, 3179-92 (2005).
7. W. Woo, H. Choo, D.W. Brown, and Z. Feng, *Metal. Mater. Trans. A* 38, 69-76 (2007).
8. C. Genevois, A. Deschamps, A. Denquin, and B. Doisneau-cottignies, Acta Mater. 53, 2447-58 (2005).
9. M. Dumount, A. Steuwer, A. Deschamps, M. Peel, and P.J. Withers, *Acta Mater.* 54, 4793-4801 (2006).
10. A. Simar, Y. Bréchet, B. de Meester, A. Denquin, and T. Pardoen, *Acta Mater.* 55, 6133-43 (2007).

11. Y. Wang, M. Chen, F. Zhou, and E. Ma, *Nature* 419, 912-15(2002).
12. R. Valiev, *Nature Mater.* 3, 511-16 (2004).
13. Y.H. Zhao, X.Z. Liao, Z. Jin, R.Z. Valiev, and Y.T. Zhu, *Acta Mater.* 52, 4589-99 (2004).
14. M.A. Krivoglaz, *Theory of X-ray and Thermal Neutron Scattering by Real Crystals*, Plenum Press, New York (1996).
15. B.D. Cullity, and S.R. Stock, *Elements of X-ray Diffraction*, Prentice Hall, Upper Saddle River (2001).
16. C. Gallais, A. Simar, D. Fabregue, A. Denquin, G. Lapasset, B. de Meester, Y. Brechet, and T. Pardoen, *Metal. Mater. Trans. A* 38, 964-81 (2007).
17. N. Afrin, D.L. Chen, X. Cao, and M. Jahazi, *Scripta Mater.* 57, 1004-07 (2007).
18. M.A.M. Bourke, D.C. Dunand, and E. Ustundag, *Appl. Phys. A*, 74, S1707-09 (2002).
19. P.J. Withers, *C. R. Physique*, 8, 806-20 (2007).
20. K. Masubuchi, *Analysis of Welded Structures*, Pergamon, New York (1980)
21. W. Woo, Z. Feng, X-L. Wang, K. An, W.B. Bailey, S.A. David, C.R. Hubbard, and H. Choo, *Residual stresses VII.* 524-525, 387-92 (2006).
22. A.C. Larson and R.B. Von Dreele, *General Structure Analysis System (GSAS)*, Rep. LAUR 86-748, Los Alamos National Laboratory, Los Alamos (2004).
23. W. Woo, Z. Feng, X-L. Wang, K. An, H. Choo, C.R. Hubbard, and S.A. David, *Appl. Phys. Lett.* 88, 248623 (2006).
24. W. Woo, Z. Feng, X-L. Wang, D.W. Brown, B. Clausen, K. An, H. Choo, C.R. Hubbard, and S.A. David, *Sci. Tech. Welding Joining* 12, 298-303 (2007).
25. T. Ungár and A. Borbély, *Appl. Phys. Lett.* 69, 3173-75 (1996).
26. T. Ungár, I. Dragomir, Á. Révész, and A. Borbély, *J. Appl. Cryst.* 32, 992-1002 (1999).
27. T. Ungár, Eötvös University, Budapest, Hungary, private communication.
28. T. Ungár, J. Gubicza, G. Ribárik, and A. Borbély, *J. Appl. Cryst.* 34, 298-310 (2001).
29. J. Gubicza, N.Q. Chinh, Z. Horita, and T.G. Langdon, *Mater. Sci. Eng. A* 387, 55-59 (2004).
30. W. Woo, L. Balogh, T. Ungár, H. Choo, and Z. Feng, *Mater. Sci. Eng. A,* 10.1016/j.msea. 2008.08.007.